YOLOv8 Deep Learning Model for Diabetic Retinopathy Fundus Image Segmentation and Disease Classification

Carlos V. G. Moura
Teleinformatics Engineering Department (DETI)
Federal University of Ceara (UFC)
Fortaleza, Brazil
carlos.victor@alu.ufc.br

Paulo C. Cortez
Teleinformatics Engineering Department (DETI)
Federal University of Ceara (UFC)
Fortaleza, Brazil
cortez@lesc.ufc.br

Débora F. Assis
Teleinformatics Engineering Department (DETI)
Federal University of Ceara (UFC)
Fortaleza, Brazil
debora.ferreira@lesc.ufc.br

Pedro C. Motta
Teleinformatics Engineering Department (DETI)
Federal University of Ceara (UFC)
Fortaleza, Brazil
pedro.motta@lesc.ufc.br

Bruno R. Silva
Teleinformatics Engineering Department (DETI)
Federal University of Ceara (UFC)
Fortaleza, Brazil
bruno@lesc.ufc.br

***Abstract*—Diabetic retinopathy (DR) is a set of retinal and vitreous changes caused by diabetes which causes visual acuity loss in its later stages, and many patients remain undiagnosed even when the disease is already causing damage. Diabetic retinopathy can be diagnosed in its earlier stages by analysis of a fundoscopy examination image, in which the ophthalmologist searches for exudates and microaneurysms, which are early lesions caused by DR. Ophthalmologists have several difficulties in providing accurate and reliable diagnoses to all patients examined. Thus, computer vision can assist ophthalmologists in diagnosing this disease using procedures such as image segmentation and classification. This work uses the YOLOv8 deep learning model to segment and classify DR retinal lesions in fundoscopy examination images using the e-ophtha dataset. Four models were trained, one segmenting and classifying exudates, other microaneurysms, and the last two segmenting both lesions together, one trained using the whole dataset, and the other trained using only the lesion images of the dataset without the healthy images. The segmentation results were quantitatively measured using the sensitivity, intersection-over-union, and DICE coefficient metrics. The exudates model obtained the best segmentation results, with 95.37% mean sensitivity and intersection-over-union and 97.62% mean DICE coefficient. The models were able to classify all images correctly between two classes, lesion and healthy, where images with one or more lesions segmented were classified as lesion images, and images without lesions were classified as healthy. The microaneurysms model obtained high median metrics results compared to its mean results, indicating that it performs close to the state-of-the-art on at least half of the testing dataset but performed worse in a few more complex cases.**

***Index Terms*—diabetic retinopathy, YOLOv8, image segmentation, image classification, deep learning**

The authors would like to thank the Brazilian National Council for Scientific and Technological Development (CNPq) under Grant No. 313599/2019-0 and Coordination of Superior Level Staff Improvement (CAPES)-Finance Code 001 for the support to this research.

I. Introduction

Diabetic retinopathy (DR) is the term used to describe a set of retinal and vitreous changes caused by diabetes, which in later stages can cause damage to visual acuity. DR is one of the leading causes of irreversible blindness, affecting around 40% of people with diabetes [1]. DR may start to develop as early as seven years before the diagnosis of type 2 diabetes, and more than 60% of type 2 diabetic patients will have some degree of retinopathy after 20 years of onset of diabetes mellitus [2]. Due to the low visual acuity often being a late symptom of DR, many patients remain undiagnosed even when the disease is already causing severe retinal damage. It can be detected by analyzing a fundoscopy examination image, where microaneurysms (red dots) or exudates (yellow dots) indicate the disease. Fundus imaging is an initial and commonly used diagnostic method due to being non-invasive, cost-efficient, and portable [3].

Kaur *et al.* [4] discuss several difficulties in the manual diagnostic of DR, such as a large number of retinal fundus images to be analyzed, which can cause ophthalmologists to misinterpret abnormalities due to fatigue. Furthermore, morphological changes in the retina are often subtle and small,

TABLE I: Related works segmentation results review

Segmentation model	**Dataset**	**Hard exudate**			**Microaneurysm**		
		SEN (%)	**DICE (%)**	**IOU (%)**	**SEN (%)**	**DICE (%)**	**IOU (%)**
Modified U-Net [8]	In-house and IDRiD	93.60	-	-	89.20	-	-
Modified U-Net [9]	e-ophtha and IDRiD	99.88	99.98	-	99.88	99.98	-
Feature Fusion U-Net [10]	IDRiD	87.55	91.38	84.14	59.33	71.88	56.10
Bayesian deep learning model [11]	IDRiD	76.7	-	-	46.40	-	-
Nested U-Net [12]	MESSIODOR and DIARETDB1	-	-	-	88.89	79.21	-
Custom CNN [14]	IDRiD	89.10	-	-	89.10	-	-
Modified U-Net [15]	IDRiD and DIARETDB1	-	-	-	80.49	86.51	76.61
Our method (YOLOv8)	**e-ophtha**	**95.37**	**97.63**	**95.37**	**80.47**	**86.32**	**80.47**

making the analysis process tedious and time-consuming, and may even cause observer variability [5]. Computer-aided diagnostic assistance to an expert is a viable method to help ophthalmologists overcome these daily difficulties, making the fundoscopy image analysis process faster and the DR diagnostics more accurate. Image segmentation and classification can be beneficial, as they can show the ophthalmologist a previous, fast indication of the possible presence and area of DR lesions in the fundoscopy image, reducing the observer variability and the chances of imprecise a diagnosis.

This work used the YOLOv8 deep learning model to segment the DR lesions and classify the images to identify the DR in fundoscopy images. There are still relatively few research works on the YOLOv8 model for medical image processing [6], even though it offers state-of-the-art results in computer vision tasks [7]. Therefore, it is necessary to research its capabilities in high-interest areas, such as medical image processing.

In this work, section 2 discusses related works about DR classification and lesion segmentation and other applications using YOLOv8 for classification and segmentation, section 3 describes the used dataset and methodology to obtain and evaluate the results, section 4 presents the obtained results and the metric evaluations, and section 5 discusses the implications and the impact of the obtained results and possible methodology that future works could follow to improve the understanding of the problem and its solution.

II. Related Works

Son *et al.* [8] obtained 93.60% and 89.20% sensitivity in hard exudate and hemorrhage segmentation, respectively, using a modified U-Net model trained on an in-house dataset and tested in the e-ophtha dataset. Sambyal et al [9] as too using a modified U-Net architecture, obtained 99.88% sensitivity and 99.98% DICE score for exudate and microaneurysm segmentation, trained on e-ophtha dataset and validated on IDRiD dataset, both datasets preprocessed. Xu *et al.* [10] obtained 87.55% and 59.33% sensitivity, 84.14% and 56.10% intersection-over-union, and 91.38% and 71.88% DICE score for hard exudate and microaneurysm segmentation respectively using Feature Fusion U-Net trained and tested on preprocessed IDRiD dataset. Garifullin *et al.* [11] obtained 76.7% and 46.4% sensitivity for hard exudate and microaneurysm segmentation respectively, using a Bayesian deep learning model trained and tested on luminosity and contrast enhanced IDRiD dataset. Kundu *et al.* [12] obtained 88.89% sensitivity and 79.21 DICE coefficient scores in red lesion segmentation using a Nested U-Net architecture based on [13], trained and tested on Contrast Limited Adaptive Histogram Equalization (CLAHE) preprocessed MESSIDOR and DIARETDB1 datasets, with a sub-image classification method for removal of false positives. Valizadeh *et al.* [14] obtained 89.10% sensitivity in DR lesion segmentation using a custom CNN after detection of the target region, trained and tested on IDRiD dataset. Skouta *et al.* [15] obtained 80.49% sensitivity, 76.61% intersection-over-union, and 86.51% DICE score in hemorrhage semantic segmentation using a custom U-Net trained on IDRiD dataset and tested on IDRiD and DIARETDB1 datasets.

From the above studies, it can be concluded that it is possible to achieve satisfactory results on DR lesion segmentation using the e-ophtha dataset for training, possibly even achieving state-of-the-art results. A summary of the best segmentation results from related work and the present work and information regarding the segmentation model and the dataset is presented in Table I.

To our best knowledge, there has been no work in the literature using YOLOv8 for the segmentation or classification of microaneurysms and exudates to detect diabetic retinopathy. The studies that used YOLOv8 for localization, segmentation and classification, with another purpose area, obtained satisfactory results. Islam et al. [16] obtained 100% classification accuracy using YOLOv8 to classify seven distinct varieties of leafy vegetables, the highest result among all used models, including YOLOv5 and YOLOv7. Phan and Nguyen [17] obtained 94.00% accuracy using YOLOv8 to detect faults in photovoltaic cells, 11% more than YOLOv7. Aboah et al. [18] obtained 92.30% precision and 90.7% recall using YOLOv8 to detect real-time multi-class helmet violation in traffic security camera images, more than YOLOv5 and YOLOv7. Ju and Cal [6] obtained 88.50% using YOLOv8 to segment bone fractures in pediatric wrist trauma x-ray images. Furthermore, the YOLOv8-seg model has achieved state-of-the-art results on various object detection, and semantic segmentation benchmarks while maintaining high speed and efficiency [7]. Thus, YOLOv8 appears to have consistently better results than its previous versions, and as it shows great potential in image classification and segmentation problems, further

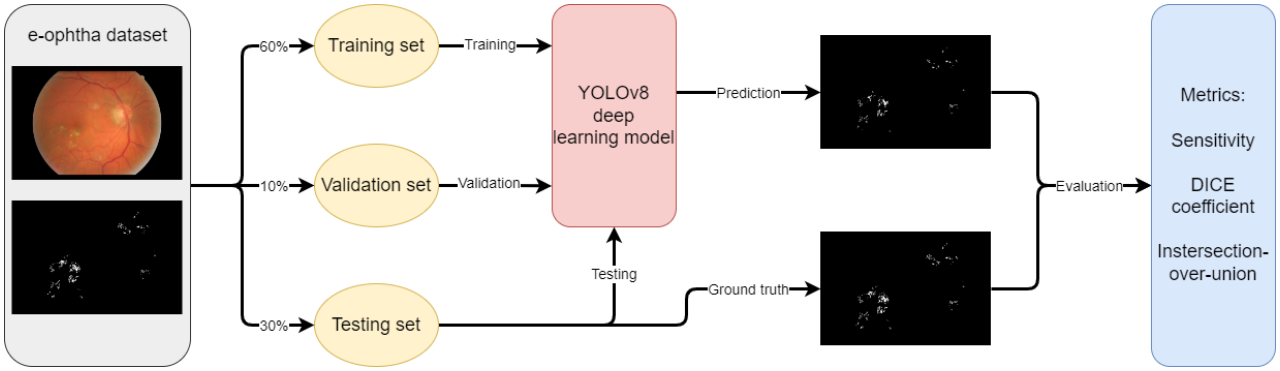

Fig. 1: Diagram of overall workflow process.

testing its capabilities in other undeveloped areas is of utmost importance.

This work evaluates the YOLOv8 segmentation and classification deep learning models in the task of detection of DR. Since we could not find previous works using YOLOv8 for this task, this work provides a significant advancement to the medical image processing area, especially the area of fundus image processing for the detection of DR, as it provides results of a yet unused deep learning model to this task and compares it to results of well knows works in the area.

III. Methods

The dataset was divided into training, validation and test sets. 60% of the dataset was set aside for the training set, 30% for the testing set, and 10% for the validation set. Images for each set were selected randomly. The division was done as such to provide the model a relevant amount of images to train, but it was necessary to use 30% of the dataset for testing to be able to evaluate the model effectively. Furthermore, four trainings were made: One with the exudate and healthy image datasets (EX model), one with the microaneurysm and healthy image datasets (MA model), one with only the exudate and microaneurysm image datasets (LS-A model), and one with the whole e-ophtha dataset, including exudate, microaneurysm and healthy image datasets (LS-B model). The LS-A and LS-B models were trained using exudate and microaneurysm image datasets as the same class, and images containing both exudates and microaneurysms had their ground truth masks fused. Each sub-dataset, test, validation, and training has the same lesion to healthy image ratio for each model. To train it was used the YOLOv8 model. The overall process of dataset preparation, segmentation and classification training, and prediction and quantitative evaluation of the results is shown in Fig 1.

The EX model has a considerably imbalanced dataset, with only 47 exudate images and 260 background (without lesion) images. The MA and LS-B models have a more reasonable lesion-to-background image ratio in the dataset, since the background set has less than twice as many images as the lesion set. However, in LS-A and LS-B models, the exudate-to-microaneurysm image ratio is also imbalanced, with 26 exudate images to 127 microaneurysm images and 21 images with both exudates and microaneurysms.

Imbalanced datasets can introduce bias and hinder the undestanding of different classes in data-driven algorithms, as well as impact the generalization capabilities of the algorithm [19]. Thus the exudate-to-background image ratio could be a possible source of error in the trained models, especially when applied to real world scenarios where the distribution of data is more diverse.

A. Dataset

The e-ophtha dataset by [20] was used for this research. E-optha is a database of color fundus images specially designed for scientific research in DR. The e-ophtha dataset consists of 413 images altogether, of which 260 are without lesions, 148 contain microaneurysms and 47 contain exudates (21 images contain both microaneurysms and exudates). The example of each class's image and ground truth mask samples from the e-ophtha dataset is presented in Fig. 2.

B. Metrics

To quantitatively analyze the experimental results, the sensitivity (SEN), DICE coefficient (DICE) and intersection-over-union (IOU) metrics were used to evaluate the performance in the task of segmenting the DR lesions. To calculate the metrics, the true positive (TP), false negative (FN) and false positive (FP) of each image were first calculated. The true positive refers to the intersection of the true lesion area and prediction lesion area, false negative refers to the intersection of the true lesion area and predicted background area (normal) area and false positive refers to the intersection of the true background area and predicted lesion area. Equation (1) shows the relation between the SEN metric and TP and FN areas. Equations (2) and (3) show the relations of the DICE and IOU metrics to TP, FP and FN areas.

$$SEN = \frac{TP}{TP + FN}, \tag{1}$$

$$DICE = \frac{2TP}{2TP + FP + FN}, \tag{2}$$

$$IOU = \frac{TP}{TP + FP + FN}, \tag{3}$$

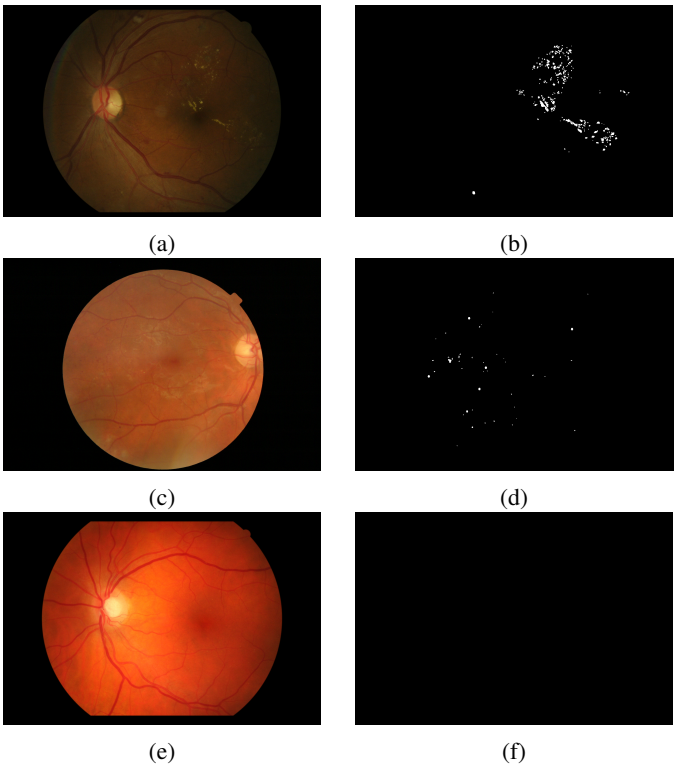

Fig. 2: E-ophtha image sample. (a) and (B) Exudate image and mask. (c) and (d) Microaneurysm image and mask. (e) and (f) Healthy image and mask.

The SEN calculates the area of overlap between predicted and ground truth masks divided by the whole mask area that should be identified as positive. It is helpful to evaluate the performance in cases where false positives are not of concern, but false negatives will incur high costs in the score. The DICE coefficient evaluates a generalized performance of the model, calculating twice the area of overlap of predicted and ground truth masks divided by the total area of both masks. However, a low DICE score can be caused by many false positives or false negatives without distinction. The IOU calculates the area of overlap between predicted and ground truth masks divided by the unified area of both masks. It gives a similar but usually lower score than the DICE coefficient. Regarding the above commonly used metrics, the closer they are to 1, the better the segmentation performance [10]. These metrics were chosen for the main reason of penalizing false negatives.

C. YOLOv8

The YOLOv8 deep learning model by [21] was used for this research. YOLOv8 is a state-of-the-art convolutional neural network architecture for object recognition and is the latest version of YOLO by Ultralytics at the time of writing. YOLOv8 can perform detection, segmentation, classification, pose estimation, and tracking. In this work, the segmentation and classification features were used.

YOLOv8 can perform real-time object detection and image segmentation. The preprocessing of images in real-time applications is usually unviable due to hardware limitations. Thus, this work evaluates the performance of YOLOv8 without dataset preprocessing due to the possibility of the development of real-time applications using YOLOv8 for diabetic retinopathy lesion segmentation.

The model parameters used to train all four models were as follows: batch size 8, image size 640 $\times$ 640 $\times$ 3, learning rate 0.01, and 50 epochs (using the best model for evaluation, not the last). The model was trained with the YOLOv8n-seg model as a base. YOLOv8n-seg is a segmentation model pretrained in the COCO dataset.

IV. Results

For each model, the SEN, IOU, and DICE coefficients were measured between the ground truth mask and the predicted mask for each image of the corresponding testing set. Then, the mean and median of the metrics results of all images of each model were calculated. The mean was chosen as it provides the average result for all images tested, and the median offers a comparative view to the mean to identify if the model provides disparate results for different groups of images. All models were evaluated for segmentation and classification at confidence level (conf) = 0.0001, as that confidence level has given the best results overall, except for the MA model, which was evaluated at conf = 0.00001.

A. Segmentation

The EX model obtained mean 95.37% and median 95.40% SEN, mean 95.37% and median 95.40% IOU, and mean 97.63% and median 97.65% DICE coefficient scores. An example image EX model prediction and the corresponding ground truth, marked over the original image, is presented in Fig. 3.

The MA model obtained mean 80.47% and median 97.69% SEN, mean 80.47% and median 97.69% IOU, and mean 86.32% and median 98.83% DICE coefficient scores. An example image MA model prediction, and the corresponding ground truth, marked over the original image, is presented in Fig. 4.

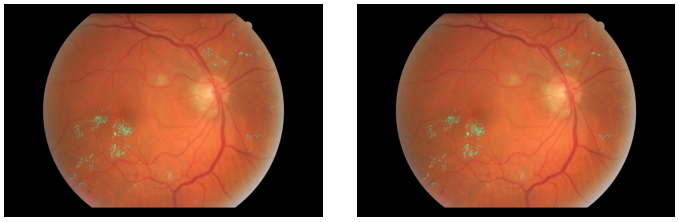

Fig. 3: EX model segmentation sample at conf = 0.0001. (a) ground truth mask. (b) predicted mask.

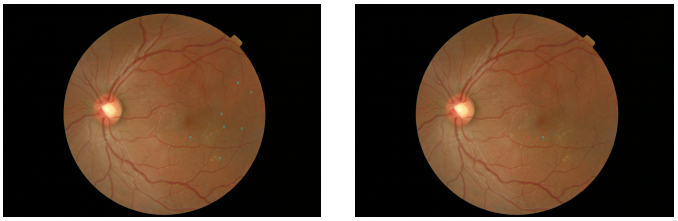

(a) (b)

Fig. 4: MA model segmentation sample at conf = 0.00001. (a) ground truth mask. (b) predicted mask.

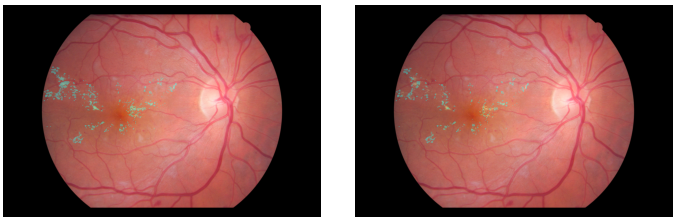

(a) (b)

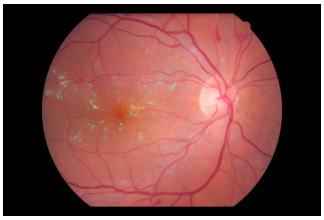

(c)

Fig. 5: LS-A and LS-B models segmentation samples at conf = 0.0001. (a) ground truth mask. (b) predicted mask for LS-A. (c) predicted mask for LS-B.

The LS-A model obtained mean 75.52% and median 81.65% SEN, mean 75.52% and median 81.65% IOU, and mean 84.46% and median 89.90% DICE coefficient scores. The LS-B model obtained mean 68.96% and median 68.87% SEN, mean 68.96% and median 68.87% IOU, and mean 79.81% and median 81.56% DICE coefficient scores. An example image LS-A and LS-B model predictions and the corresponding ground truth, marked over the original image, is presented in Fig. 5.

The EX model obtained the best segmentation metrics results by far, even being close to a state-of-the-art exudate segmentation model, as its results were superior to most of the related works models, even being trained in an imbalanced dataset and without preprocessing to improve the model's performance. The EX model obtained higher metric values than all related works' models observed, with the sole exception of the modified U-Net proposed by [9].

The LS-A model obtained better results than the LS-B model. Still, both models obtained competitive results to the related works observed, considering both hard exudate and microaneurysm segmentation results. Since the LS-A and LS-B results were average and the models don't differentiate between exudates and microaneurysms in fundus images, they may not be the best choice for assisting professionals in diagnosing DR. The MA model obtained a higher mean IOU score than all microaneurysm segmenting models observed, and its SEN and IOU mean scores were competitive with the related works. However, the MA model obtained considerably higher median metric values than the mean values, which can lead to the conclusion that it performed close to the state-of-the-art in more than half of the testing data, but some small number of harder to segment images dragged the mean value down. It is possible that with a preprocessing technique added to the workflow, the MA model's results can be improved in these more complex cases since the microaneurysms are very similar to the background of the fundus images [15]. The metrics results for each segmentation model are presented in table II.

TABLE II: Segmentation models metrics results

Model	SEN (%)		IOU (%)		DICE (%)	
	Mean	Median	Mean	Median	Mean	Median
EX	95.37	95.40	95.37	95.40	97.63	97.65
LS-A	75.52	81.65	75.52	81.65	84.46	89.90
LS-B	68.96	68.87	68.96	68.87	79.81	81.56
MA	80.47	97.69	80.47	97.69	86.32	98.83

Furthermore, the equal SEN and IOU metrics in every model show that no false positives were predicted. This indicates that, even if the model performance is already high, it can still be improved to detect more lesions, as there may be room to increase the segmented area without increasing the number of FPs.

B. Classification

Considering classifying the images into two classes, lesion and healthy, the EX and MA models could classify all images correctly without any false positives or negatives. The EX and MA models have 15 and 45 lesion class images respectively, and 78 healthy class images in their testing datasets. The LS-A model could classify all images correctly, but the LS-B model classified two lesion images as healthy. The LS-A and LS-B models have 53 lesion class images and 77 healthy class images in their testing datasets. All models' confusion matrices, where images with one or more lesions segmented were classified as lesion images, and images without lesions were classified as healthy, are shown in Fig. 6.

Both EX, MA, and LS-A models were able to classify every image correctly, which indicates a high precision of classification of the YOLOv8 model, even if the MA and LS-A model has considerably worse mean segmentation metrics results compared to the EX model. The LS-B model classified almost all images correctly. However, it misinterpreted two lesion images as healthy images, which in medical imaging can be a fatal error, as DR patients could be wrongly diagnosed as healthy.

(a) (b) (c) (d)

Fig. 6: Confusion matrices of each model. (a) EX model at conf = 0.0001. (B) MA model at conf = 0.00001. (c) LS-A model at conf = 0.0001 (d) LS-B model at conf = 0.0001.

V. Conclusion

The analysis of fundoscopy examination images is important in diagnosing diabetic retinopathy. In this work, the YOLOv8 segmentation model was able to segment exudates with great results as compared to previous works techniques, even without the use of preprocessing in the training dataset. The model could also correctly classify all images between DR affected and healthy, including exudate and microaneurysm images. The model could also segment microaneurysms with competitive results compared to previous works. However, it scored a much higher median than mean in this task, indicating that it performs close to the state-of-the-art in at least half of the testing images but performs worst on a small number of more complex cases.

It is clear from the results that YOLOv8 offers excellent potential in medical image processing applications, as it outperformed previous methods in the measured metrics. Therefore, the presented method will help assist ophthalmologists in diagnosing diabetic retinopathy by both classifying the images and segmenting microaneurysms with high accuracy.

Using preprocessing to enhance red lesions in the images could make the model consistently segment microaneurysms with results similar to or better than previous works, as was done with exudates. Further research in image preprocessing to enhance YOLOv8 segmentation results is necessary to explore all the model's potential in the task of segmenting DR. Further research must also be made to evaluate YOLOv8 segmentation and classification in other DR image datasets, as well as segment and classify more DR lesion classes to differentiate various stages of the disease.

Acknowledgment

This work was made possible with the financial support of the Coordination of Superior Level Staff Improvement (CAPES), and with the support of the Laboratory of Computer Systems Engineering (LESC) - UFC.

References

[1] M. B. Nehemy. Retinopatia diabética. Arq. Brasil. Oftal. 61(3), 1998.

[2] H. A. Keenan, T. Costacou, J. K. Sun, A. Doria, J. Cavellerano, J. Coney, T. J. Orchard, L. P. Aiello and G. L. King. Clinical factors associated with resistance to microvascular complications in diabetic patients of extreme disease duration. The 50-Year Medalist Study. Diabetes Care, 30, 2007. http://dx.doi.org/10.2337/dc06-2222

[3] K. R. Khaderi, K. A. Ahmed, J. L. Berry, L. T. Labriola and R. Cornwell. Retinal imaging modalities: advantages and limitations for clinical practice. Retin Physician. https://www.retinalphysician.com/issues/2011/april-2011/retinal-imaging-modalities-advantages-and-limitat. Accessed 11 June 2023.

[4] J. Kaur, D. Mittal and R. Singla. Diabetic retinopathy diagnosis through computer-aided fundus image analysis: a review. CIMNE, Barcelona, Spain 2021.

[5] M. R. K. Mookiah, U. R. Acharya, C. K. Chua, C. M. Lim, E. Y. K. Ng and A. Laude. Computer-aided diagnosis of diabetic retinopathy: a review. Computers in Biology and Medicine, Volume 43, Issue 12, 1 December 2013, Pages 2136-2155.

[6] R. Ju and W. Cal. Fracture detection in pediatric wrist trauma x-ray images using YOLOv8 algorithm. arXiv:2304.05071v3 [cs.CV]. https://doi.org/10.48550/arXiv.2304.05071. Accessed in 17 June 2023. Unpublished.

[7] J. R. Terven and D. M. Cordova-Esparaza. A comprehencise review of YOLO: from YOLOv1 and beyond. arXiv:2304.00501v3 [cs.CV]. https://doi.org/10.48550/arXiv.2304.00501. Accessed 17 June 2023. Unpublished.

[8] J. Son, J. Y. Shin, H. D. Kim, K. Jung, K. H. Park, S. J. Park. Development and validation of deep learning models for screening multiple abnormal findings in retinal fundus images. Ophthalmology, Volume 127, Issue 1, January 2020, Pages 85–94

[9] N. Sambyal, P. Saini, R. Syal and V. Gupta. Modified U-Net architecture for semantic segmentation of diabetic retinopathy images. Biocybernetics and Biomedical Engineering. Volume 40, Issue 3, July–September 2020, Pages 1094-1109.

[10] Y. Xu, Z. Zhou, X. Li, N. Zhang, M. Zhang and P. Wei. FFU-Net: feature fusion U-Net for lesion segmentation of diabetic retinopathy. Artificial Intelligence for Medical Image Analysis. Volume 2021, Article ID 6644071, 12 pages, 2021. https://doi.org/10.1155/2021/6644071. Accessed 12 June 2023.

[11] A. Garifullin, L. Lensu and H. Uusitalo. Deep Bayesian baseline for segmenting diabetic retinopathy lesions: advances and challenges. Computers in Biology and Medicine, Volume 136, 2021, 104725, ISSN 0010-4825, https://doi.org/10.1016/j.compbiomed.2021.104725. Accessed 13 June 2023.

[12] S. Kundu, V. Karale, G. Ghorai, G. Sarkar, S. Ghosh and A. K. Dhara. Nested u-net for segmentation of red lesions in retinal fundus images and sub-image classification for removal of false positives. Journal of Digital Imaging 35, 1111–1119, 2022. https://doi.org/10.1007/s10278-022-00629-4. Accessed in 17 June 2023.

[13] Z. Zhou, M. M. R. Siddiquee, N. Tajbakhsh and J. Liang. A nested u-net architecture for medical image segmentation. Deep Learning in Medical Image Analysis and Multimodal Learning for Clinical Decision Support, pages 3–11. Springer, 2018.

[14] A. Valizadeh, S. J. Ghoushchi, R. Ranjbarzadeh and Y. Pourasad. Presentation of a segmentation method for a diabetic retinopathy patient's fundus region detection using a convolutional neural network. Hindawi, Computational Intelligence and Neuroscience, Volume 2021, Article ID 7714351, 14 pages, 2021.

[15] A. Skouta, A. Elmoufidi, S. Jai-Andaloussi and O. Ouchetto. Hemorrhage semantic segmentation if fundus images for the diagnosis of diabetic retinopathy by using a convolutional neural network. Journal of Big Data 9, 78, 2022.

[16] A. Islam, S. R. S. Raisa and N. H. Khan. Enhanced leafy vegetable analysis: image classification and disease instance segmentation using deep learning techniques. SSRN, 2023.

[17] Q. B. Phan and T. Nguyen. A novel approach for PV cell fault detection using YOLOv8 and particle swarm optimization. TechRxiv. Preprint. https://doi.org/10.36227/techrxiv.22680484.v1. Accessed 11 June 2023.

[18] A. Aboah, B. Wang, U. Bagci and Y. Adu-Gyamfi. Real-time multi-class helmet violation detection using few-shot data sampling technique and YOLOv8. Proceedings of the IEEE/CVF Conference on Computer Vision and Pattern Recognition (CVPR) Workshops, 2023, pp. 5349-5357.

[19] P. Ruiz-Ponce, D. Ortiz-Perez, J. Garcia-Rodriguez and B. Kiefer. POSEIDON: A data augmentation tool for small object detection datasets in maritime environments. Sensors 2023, 23(7), 3691; https://doi.org/10.3390/s23073691. Accessed 30 August 2023.

[20] E. Decencière, G. Cazuguel, X.Zhang, G. Thibault, J.-C. Klein, F. Meyer, B. Marcotegui, G. Quellec, M. Lamard, R. Danno, D. Elie, P. Massin, Z. Viktor, A. Erginay, B. Laÿ, A. Chabouis. TeleOphta: machine learning and image processing methods for teleophthalmology. IRBM, 2013.

[21] G. Jocher, A. Chaurasia and J. Qiu. YOLO by Ultralytics (Version 8.0.0) [Computer software]. 2023. https://github.com/ultralytics/ultralytics